

Article

Effects of Tip Leakage Vortex Cavitation on Flow Field under Cavitation Instability

Youngkuk Yoon  and Seung Jin Song *

Department of Mechanical Engineering, Seoul National University, Seoul 08826, Republic of Korea; truesky1218@snu.ac.kr

* Correspondence: sjsong@snu.ac.kr

Abstract: Cavitation instabilities can induce axial and circumferential vibrations, as well as noise in turbopump inducers. Therefore, the purpose of the present study is to investigate the mechanism of cavitation instability. The flow field near the two-bladed inducer leading edge under alternate blade cavitation was experimentally investigated using particle image velocimetry (PIV). It was found that the tip leakage vortex cavitation draws the flow toward its region of collapse and induces a negative change in the incidence to the adjacent blade. Moreover, this blade-to-blade interaction was identified as the main cause of alternate blade cavitation. Furthermore, it was demonstrated that this blade-to-blade interaction is strongest when the cavity collapse occurs in the inducer throat area, where the leading edge of the following blade is located.

Keywords: turbopump inducer; cavitation instability; particle image velocimetry (PIV)



Citation: Yoon, Y.; Song, S.J. Effects of Tip Leakage Vortex Cavitation on Flow Field under Cavitation Instability. *Int. J. Turbomach. Propuls. Power* **2023**, *8*, 17. <https://doi.org/10.3390/ijtp8020017>

Academic Editors: János Gábor Vad, Csaba Horváth and Tamás Benedek

Received: 13 February 2023

Revised: 18 April 2023

Accepted: 4 May 2023

Published: 1 June 2023



Copyright: © 2023 by the authors. Licensee MDPI, Basel, Switzerland. This article is an open access article distributed under the terms and conditions of the Creative Commons Attribution (CC BY-NC-ND) license (<https://creativecommons.org/licenses/by-nc-nd/4.0/>).

1. Introduction

Inducer cavitation instabilities can cause serious noise and vibration, which may result in the failure of the propulsion system. Therefore, their types and identification have received significant attention. For instance, Tsujimoto et al. [1] observed various cavitation instabilities that occurred in a three-bladed inducer and categorized them into local instabilities such as super-synchronous rotating cavitation and global instabilities such as cavitation surge. Similarly, Cervone et al. [2] experimentally observed a cavitation instability called alternate blade cavitation in a two-bladed inducer. These various cavitation instabilities have different frequency and spatial mode characteristics, which can be identified using Fourier transformation and circumferential unsteady pressure measurements.

Various analytical models have been suggested to predict cavitation instability and analyze its mechanism. Tsujimoto et al. [3] used an actuator disk method to predict rotating cavitation, where quasi-steady lumped parameters, such as mass flow gain factor and cavitation compliance, were introduced. The study showed that the mass flow gain factor plays a key role in the cavitation instability. Similarly, Watanabe et al. [4] and Horiguchi et al. [5] performed stability analysis using the singularity method, predicting various cavitation instabilities, including forward and backward propagating rotating cavitation. However, these methods cannot adequately reflect the 3-D nature of the inducer cavitation, which is primarily composed of tip leakage vortex cavitation (TLVC). Previous studies showed TLVC has a highly complex 3-D structure including severe turbulence, rather than having a quasi-steady feature with glossy surfaces which can be observed in 2-D sheet-type cavities. Cheng et al. [6] suggested the development of the TLVC would significantly alter the vorticity and turbulence kinetic energy distribution of the flow field, and due to the complex flow features, there is still no simple way to control the TLVC. Also, Cheng et al. [7] performed a Large Eddy Simulation (LES) and showed that the large amount of turbulent kinetic energy is produced around the TLVC region due to the interaction between three different vortex structures (tip leakage vortex, tip separation vortex, and induced vortex).

Hence, 3-D numerical approaches and experiments have been conducted to investigate the cavitation instability mechanism. For instance, Kang et al. [8] conducted 3-D numerical simulations, showing that cavitation instabilities begin to occur when the cavity on a blade interacts with the adjacent blade leading edge. Additionally, Kim and Song [9] performed an experimental investigation on rotating cavitation, demonstrating that cavitation reduces the incidence of the following blade using particle image velocimetry (PIV) and high-speed visualization. Nevertheless, although these studies proposed the mechanism of blade-to-blade interaction for cavitation instability, only a few selected cases have been examined in the research.

Therefore, the present research investigates the interaction between the cavity and the flow field under various operating conditions for a two-bladed inducer, using PIV to quantify the change in the velocity field around the blade leading edge. Furthermore, the study aims to analyze the blade-to-blade interaction under alternate blade cavitation.

2. Experimental Setup

Experiments were conducted in the Seoul National University Water Tunnel (SNU-WT), as schematically shown in Figure 1. The SNU-WT comprises a water tank, electric heater, flow meter, booster pump, control valve, and an inducer test section, which enables the independent control of flow coefficient and cavitation number. Moreover, to prevent particles larger than 1 micron from entering the test facility, a filtration chamber was incorporated. For a detailed description of the facility, refer to Kim and Song [9].

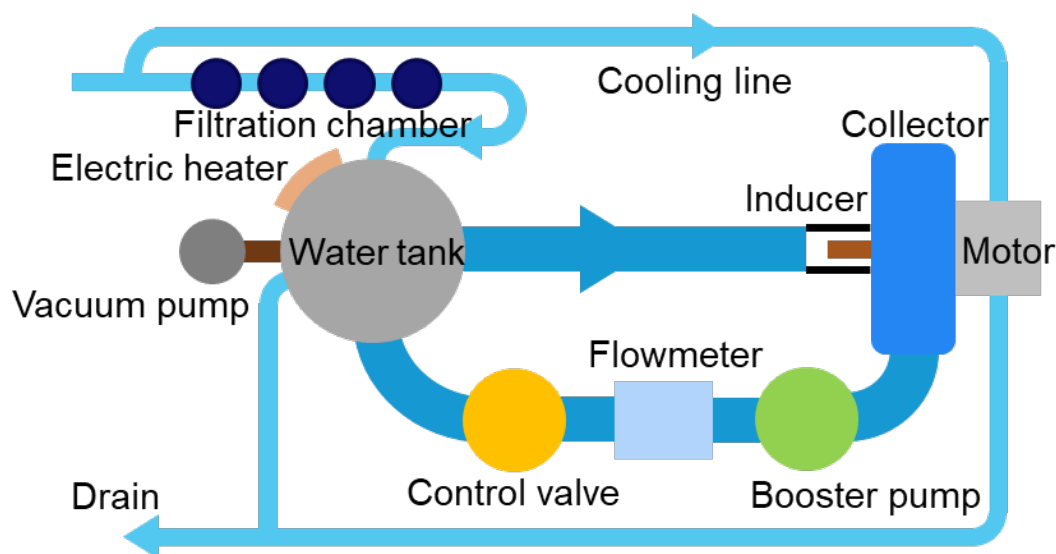


Figure 1. Schematic diagram of Seoul National University Water Tunnel.

To determine the cavitation number and identify cavitation instability, both steady and unsteady pressure measurements were performed. Four pneumatic pressure sensors (Druck PMP 5073) were mounted at the inlet and outlet of the inducer, while five unsteady pressure transducers (Kulite HKM-375) were flush-mounted at the inducer inlet casing. In addition, for the PIV measurement, the inducer casing was constructed using transparent acrylic. The flow field was measured using a Litron L 200-15 PIV laser and a Phantom v2640 camera.

In the present study, a two-bladed inducer (Figure 2) was examined. Details about the inducer can be found in [10]. All experiments were conducted under the design flow coefficient, and the cavitation number was gradually reduced from the non-cavitating condition to a near super-cavitating condition, which induced severe alternate blade cavitation.

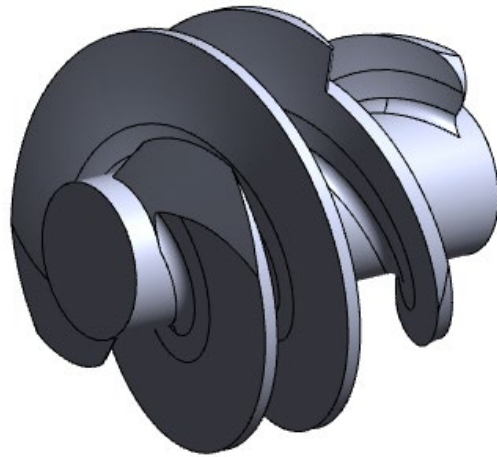


Figure 2. Geometry of the test inducer.

3. Experiment Results and Discussion

To quantify the blade-to-blade interaction, the flow field near the blade leading edge was obtained under non-cavitating conditions and averaged over a region of interest, as shown in Figure 3.

The background image in Figure 3 is a raw image captured under continuous lighting using a high-speed camera. Overlapped particle images were obtained under pulsed laser lighting, and the resulting velocity vectors are shown in green. The red dotted box indicates the area over which the velocity vectors were averaged to determine the mean velocity vector near the blade leading edge.

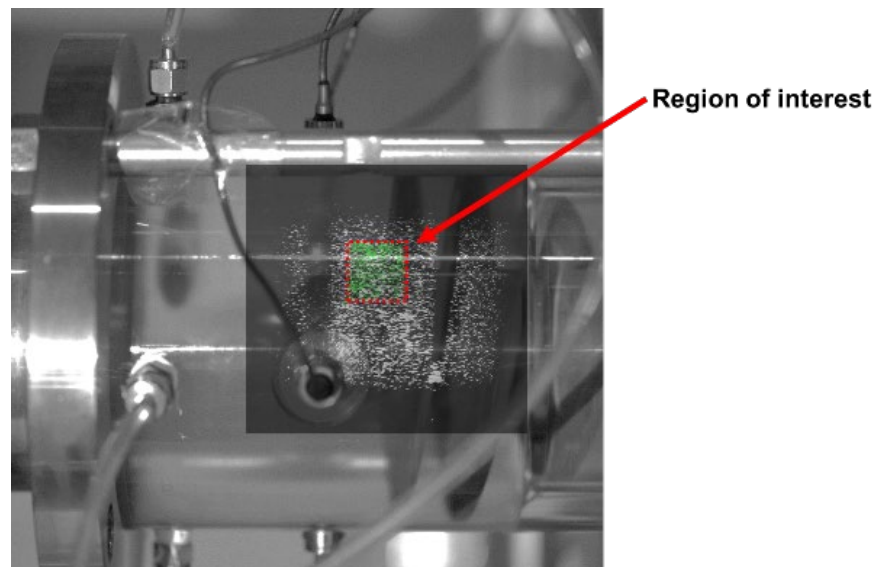


Figure 3. PIV region of interest.

At the cavitating condition, the same calculation was performed, and the difference between the mean velocity vectors was obtained. Under alternate blade cavitation, the leading edges of the two blades were treated separately due to the asymmetry of the cavity. Finally, these velocity differences were converted to changes in the incidence in the rotating frame, $\Delta\alpha$. In the present study, $\Delta\alpha$ was used to represent the blade-to-blade interaction. (In this study, incidence $(\alpha_1 - \alpha_1')$, which is defined as the difference between the flow angle (α_1) and the blade angle (α_1') , was used instead of angle of attack. Although the numerical difference between the two values is small due to the small camber angle of the inducer blade, incidence is more suitable for the turbomachinery analysis conducted in this paper).

In this study, the occurrence of alternate blade cavitation was examined using unsteady pressure measurements at the inducer casing inlet. At a distance of $0.15 D$ upstream of the inducer tip leading edge (where D is the inducer casing diameter), an unsteady pressure transducer was flush-mounted, and the data was sampled at 2000 samples per second. As the cavitation number was decreased during the experiment, the unsteady pressure signal, with its DC component filtered out, was Fourier-transformed to examine the alternate blade cavitation. The results of the Fourier transformation are shown in Figures 4 and 5 for equal length cavitation and alternate blade cavitation, respectively. In both cases, a peak was observed at a normalized frequency of 2 due to the blade passing frequency of the two-bladed inducer. However, if the system was under alternate blade cavitation, as shown in Figure 5, a peak at a normalized frequency of 1 (which equals the shaft rotating frequency) was excited due to the asymmetry of the alternate blade cavitation. Figure 6 visually demonstrates the asymmetry of cavity development under alternate blade cavitation, where both long and short cavities are developed on different blades, forming an asymmetric pattern that remains stationary in the rotating frame. Therefore, the peak at a normalized frequency of 1 was used to judge whether the alternate blade cavitation occurred, and its magnitude represented the strength of the instability. In the experiment, both the magnitude of the Fourier coefficient and the difference between the two cavity lengths showed the same trend, and thus both were used to represent the magnitude of the alternate blade cavitation.

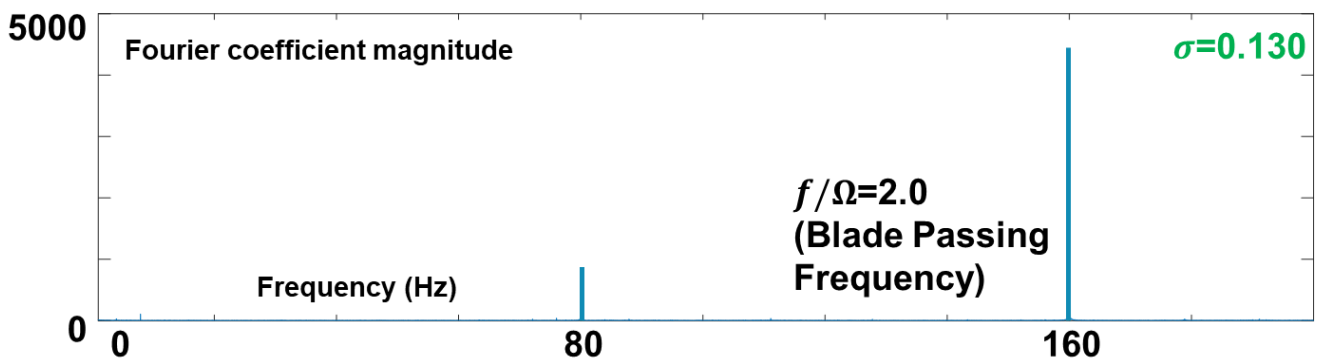


Figure 4. Typical frequency traces under equal length cavitation.

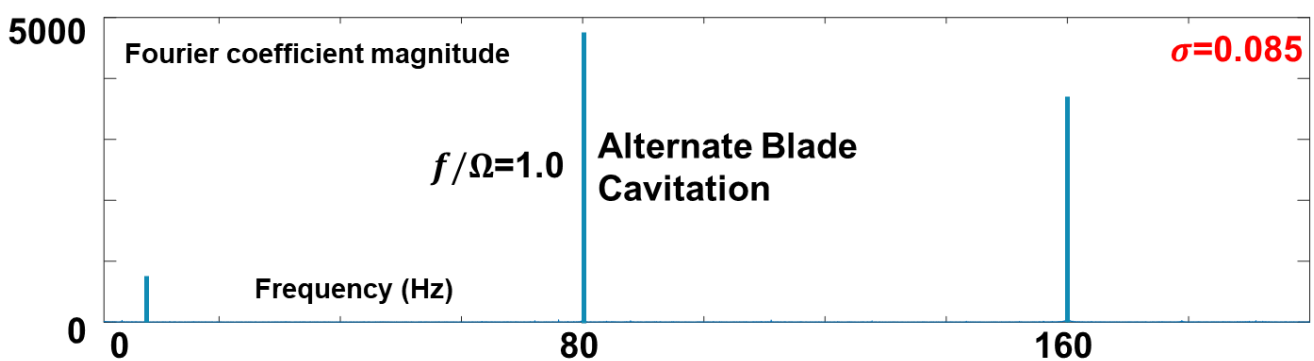


Figure 5. Typical frequency traces under two-bladed inducer alternate blade cavitation.

Figure 6 also shows the 3-D nature of the cavity on the current inducer. Due to the back-swept leading edge of the inducer, 2-D sheet-type cavity at the hub region is suppressed, and most of the cavity is developed at the tip region. At the tip region, pressure difference between the pressure side and suction side of the blade drives the fluid to go through the tip clearance. This tip clearance flow creates a shear layer with the main flow and, consequently, vortex is generated (tip clearance vortex). While low pressure region is created at the vortex core, cavitation occurs inside the vortex (TLVC). Additionally, TLVC shows highly intermittent behavior because of the large turbulent kinetic energy at the

vortex region [5,6]. Thus, rather than glossy surface, bubbly surface is observed as a bright region from the high-speed visualization. Cavitation at the tip separation vortex region shown in the right side of Figure 6 further indicate the tip clearance flow is the main source of cavitation for the test inducer.

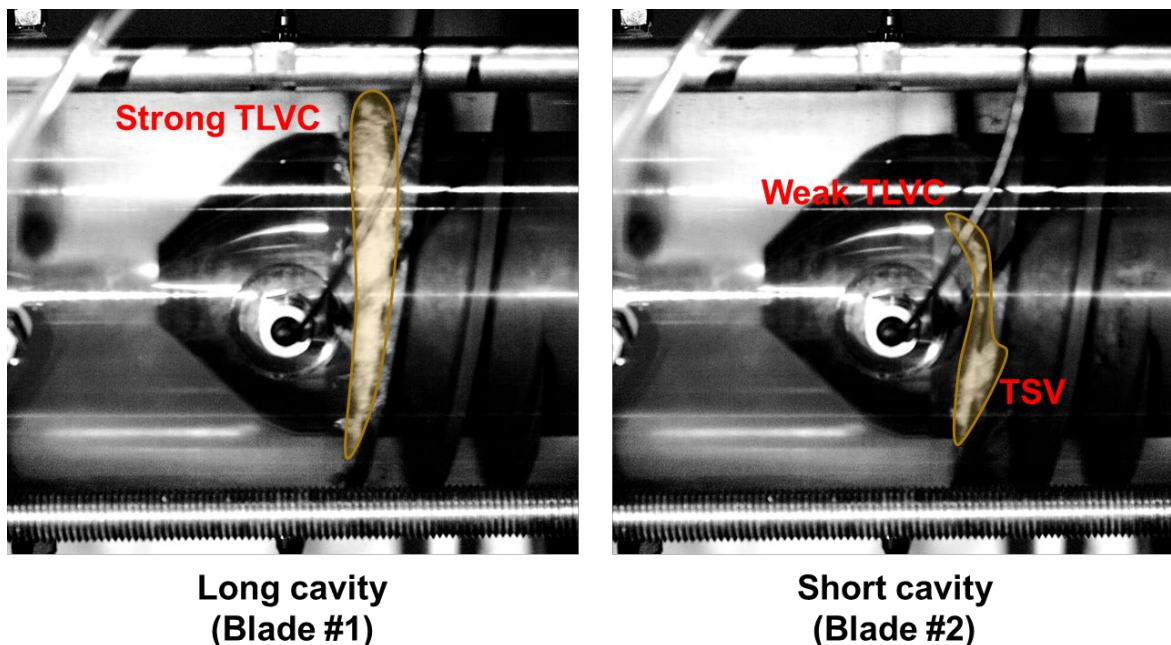


Figure 6. Visualization of alternate blade cavitation.

Due to the strong axial flow induced by the collapsing cavity, $\Delta\alpha$ has a negative sign in most situations. Figures 7–9 show the flow field vector plots at the PIV region of interest under non-cavitating conditions and alternate blade cavitation. The x -axis and the y -axis of the vector plots are normalized with the width and height of the region of interest (shown in Figure 3). Thus, the square defined by the coordinate (0,0) and (1,1) corresponds to the entire region of interest. In Figures 8 and 9, both blades 1 and 2 are shown to compare the effect of the larger and smaller cavities. In Figure 7, it can be seen that backflow is developed near the blade leading edge due to the adverse pressure gradient of the inducer. In Figure 8, a similar flow structure is developed near the blade 1 leading edge (blades are numbered as 1 and 2, corresponding to the blade with larger cavity and smaller cavity under alternate blade cavitation, respectively). Therefore, the smaller cavity induced at blade 2 is not developed enough to interact with the leading edge of the following blade.

However, as shown in Figure 9, a strong axial flow is developed at the leading edge of blade 2. This is a result of the cavity collapse occurring near the leading edge of blade 2. The cavity developed at blade 1 is large enough to interact with the following blade's leading edge. Therefore, it collapses due to high pressure at the throat area and drags the surrounding fluid to create a strong axial flow. This axial flow reduces the incidence of the following blade and inhibits the cavity development.

The existence of a critical cavity length that enables the cavity to interact with the following blade leading edge can also be confirmed during the early stages of cavity development. At the cavitation number of 0.130 and 0.115, the normalized cavity length is less than 0.5, and the cavity develops in the form of equal length cavitation (the same cavity develops at both blades). Figures 10 and 11 visualize the cavity in both cavitation numbers. It can be seen that the cavities are not large enough to reach the following blade's leading edge, and no impact is exerted on the incidence. With respect to the following blade, those cavities are the same as the non-cavitating condition.

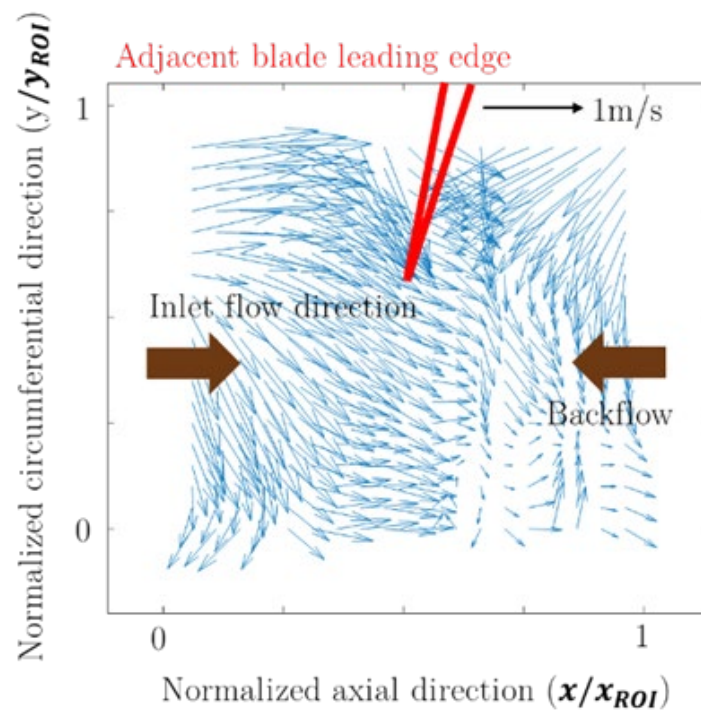


Figure 7. Flow field near blade leading edge at non-cavitating condition.

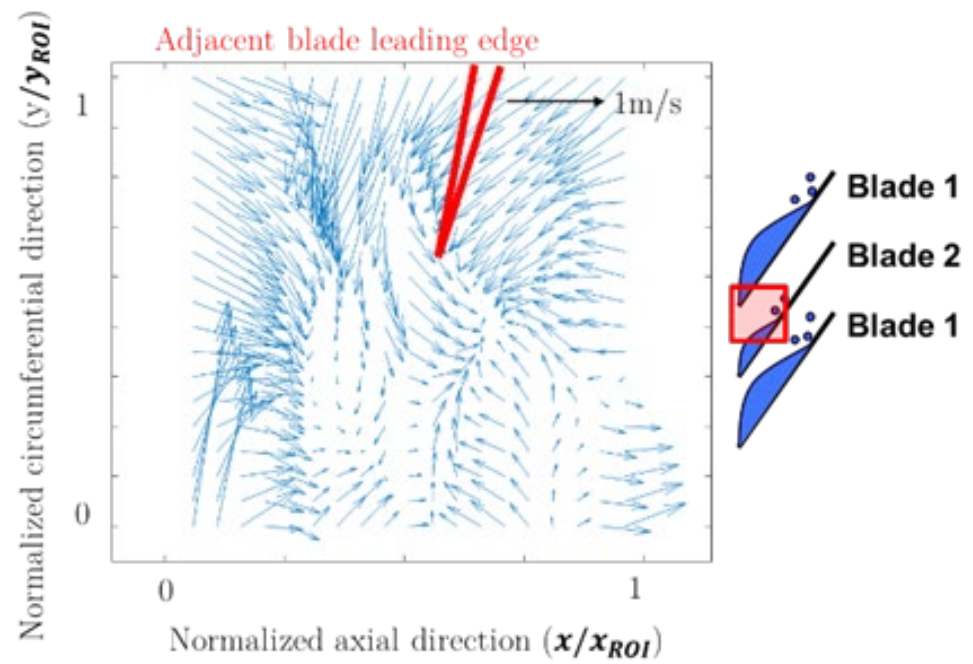


Figure 8. Flow field near blade 1 leading edge during alternate blade cavitation.

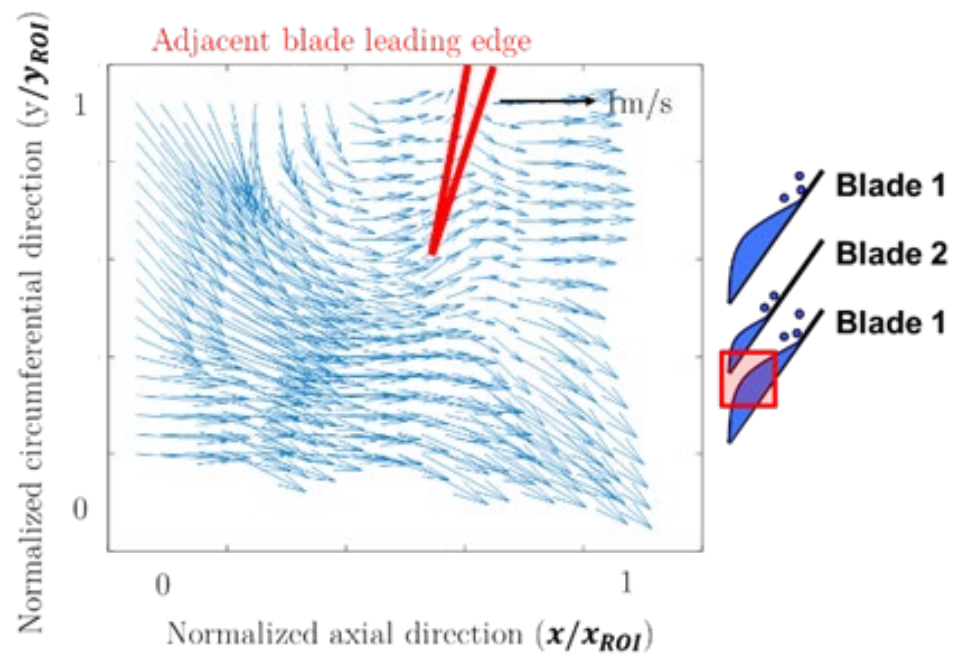


Figure 9. Flow field near blade 2 leading edge during alternate blade cavitation.

Figure 12 summarizes the experiment results under various cavitation numbers, which is defined as follows:

$$\sigma = \frac{p_{inlet} - p_v}{\frac{1}{2}\rho U_{tip}^2}. \tag{1}$$

The ordinate of Figure 12 is the normalized cavity length, which is the length of the cavity divided by the inducer throat chord length, as illustrated in the right inset of Figure 12. As the cavitation number drops below 0.110, the cavity length graph bifurcates, and the maximum difference occurs at approximately $\sigma = 0.085$. The red line represents the longer cavity length, while the blue line represents the shorter one. Figure 12 demonstrates that, after the onset of alternate blade cavitation, the magnitude (or difference between the two cavity lengths) increases until it reaches a certain cavitation number, after which it starts to decrease again.

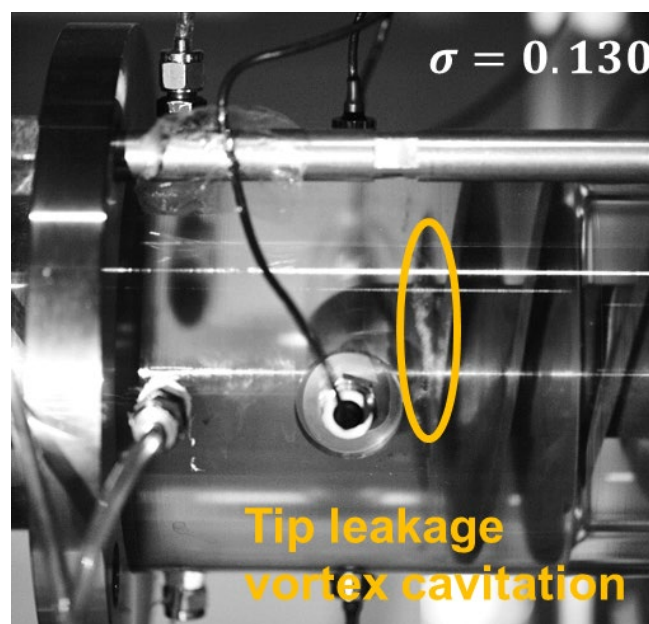


Figure 10. High-speed visualization of the cavity at $\sigma = 0.130$.

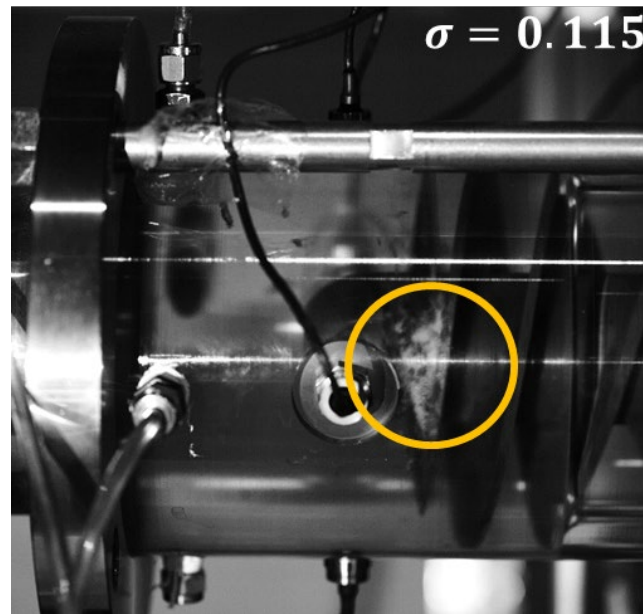


Figure 11. High-speed visualization of the cavity at $\sigma = 0.115$.

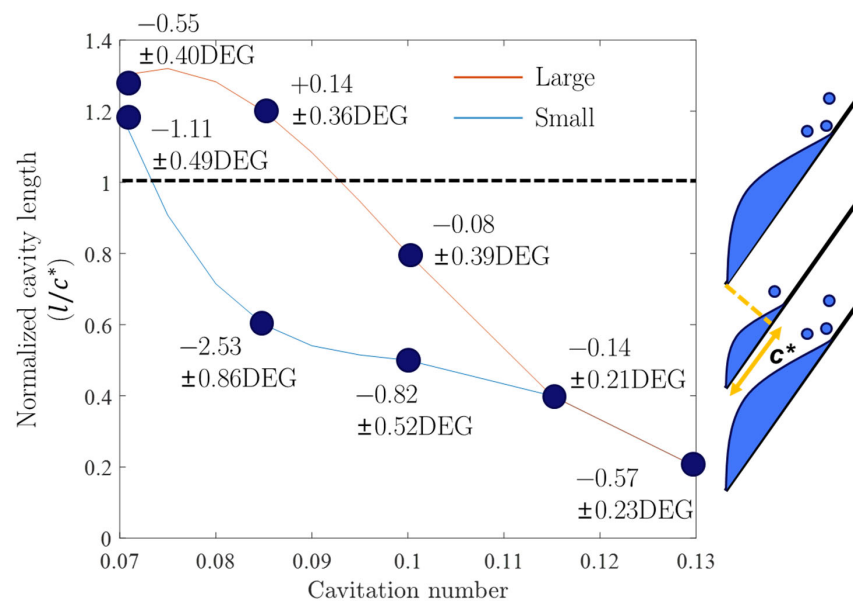


Figure 12. Cavity length and change in incidence under various cavitation number.

The dark blue dots and captions in Figure 12 represent $\Delta\alpha$ s at the given cavitation number and blade. The alternate blade cavitation is caused by uneven incidence for each blade, as shown in Figures 8 and 9. The cavity on the red branch is large enough to interact with the leading edge of the following blade, and it induces strong axial flow, leading to a decrease in the incidence of the following blade. As a result, the blade loading of the following blade (blue branch) decreases, and the tip leakage vortex cavitation (TLVC) extent also decreases. The measured $\Delta\alpha$ s at various cavitation numbers can explain the changing magnitude of the alternate blade cavitation, as also observed by Huang et al. [11]. The alternate blade cavitation reaches its maximum magnitude when the normalized length of the larger cavity is around 1. The decrease in incidence due to the larger cavity becomes smaller before and after that point. Therefore, it can be concluded that the magnitude of $\Delta\alpha$ is at its highest when the normalized cavity length is close to 1 ($l \approx c^*$, where c^* is the chord length between the leading edge of the blade and the throat). As the cavitation number decreases, the cavity length increases, resulting in an increase in the magnitude

of $\Delta\alpha$ and the alternate blade cavitation until the cavity length reaches c^* . Once the cavity length reaches c^* , $\Delta\alpha$ and the alternate blade cavitation start to decrease.

Physically, the maximized $\Delta\alpha$ at $l \approx c^*$ can be explained by the position of cavity collapse. When the cavity bubble at the TLVC trailing edge collapses, it induces a large axial flow and decreases the incidence of the following blade. According to Kang et al. [8], the position of the TLVC trailing edge plays a key role. Therefore, if the position of the cavity collapse coincides with the leading edge of the following blade, $\Delta\alpha$ is maximized, and the alternate blade cavitation becomes the strongest. This can be seen more clearly in Figures 13 and 14. Figure 13 shows a larger cavity at $\sigma = 0.085$, and Figure 14 shows a larger cavity at $\sigma = 0.070$. At $\sigma = 0.085$, most of the cavities collapse near the leading edge of the following blade. However, at $\sigma = 0.070$, the TLVC extends further until $l/c^* = 1.3$, and much fewer cavities collapse near the leading edge of the following blade. This reduces the induced axial flow and, accordingly, decreases the incidence of the following blade less.

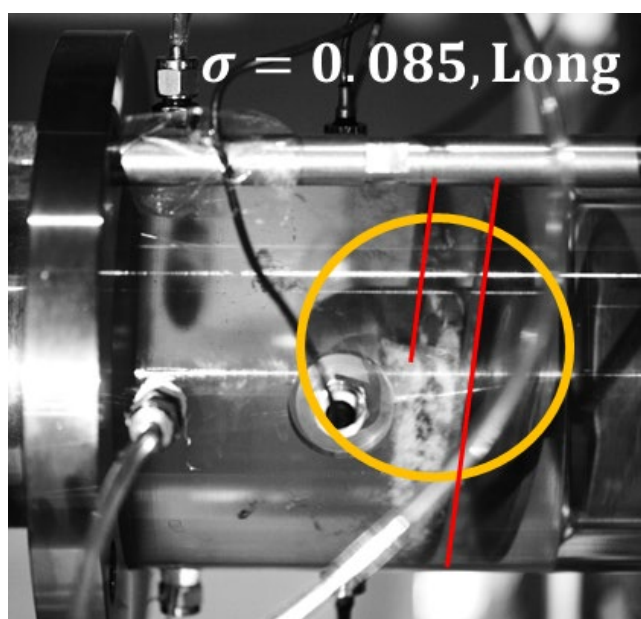


Figure 13. Visualization of the cavity at $\sigma = 0.085$.

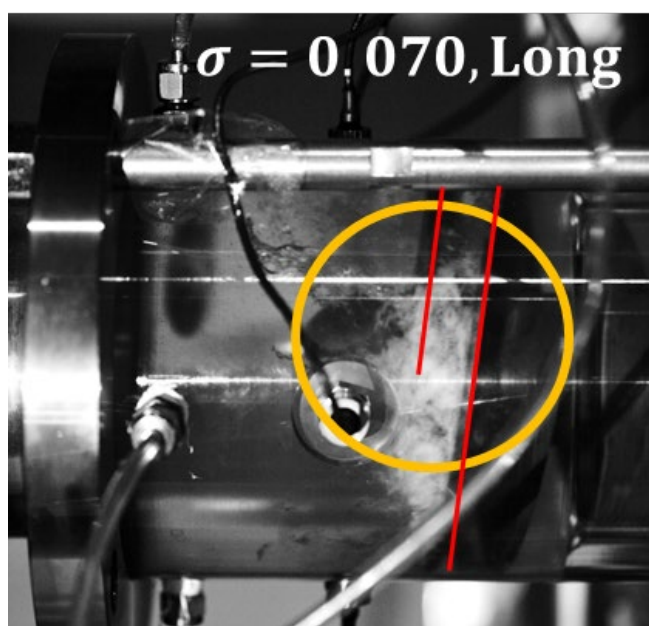


Figure 14. Visualization of the cavity at $\sigma = 0.070$.

4. Summary and Conclusions

In summary, this study explores the relationship between cavity and its interaction with the following blade in a two-bladed inducer. The study employs experimental techniques such as PIV and high-speed visualization of the cavity to quantify the interaction and its effects on the TLVC extent of the following blade. The results show that the cavity collapse decreases the incidence of the following blade, resulting in alternate blade cavitation. The study further explains that the maximum magnitude of alternate blade cavitation occurs when the normalized cavity length is around 1 and the cavity collapses near the following blade leading edge.

Author Contributions: Conceptualization, Y.Y. and S.J.S.; Methodology, Y.Y.; Software, Y.Y.; Validation, Y.Y.; Formal Analysis, Y.Y.; Investigation, Y.Y.; Resources, S.J.S.; Data Curation, Y.Y.; Writing—Original Draft Preparation, Y.Y.; Writing—Review & Editing, Y.Y. and S.J.S.; Visualization, Y.Y.; Supervision, S.J.S.; Project Administration, S.J.S.; Funding Acquisition, S.J.S. All authors have read and agreed to the published version of the manuscript.

Funding: This research received no external funding.

Institutional Review Board Statement: Not applicable.

Informed Consent Statement: Not applicable.

Data Availability Statement: Not applicable.

Acknowledgments: This work was supported by BK21+ Program and Seoul National University Institute of Advanced Machines and Design (SNU-IAMD).

Conflicts of Interest: The authors declare no conflict of interest.

References

1. Tsujimoto, Y.; Yoshida, Y.; Maekawa, Y.; Watanabe, S.; Hashimoto, T. Observation of Oscillating Cavitation of an Inducer. *J. Fluids Eng. Trans. ASME* **1997**, *119*, 775–781. [[CrossRef](#)]
2. Cervone, A.; Bramanti, C.; Rapposelli, E.; Torre, L.; d’Agostino, L. Experimental Characterization of Cavitation Instabilities in a Two-Bladed Axial Inducer. *J. Propuls. Power* **2006**, *22*, 1389–1395. [[CrossRef](#)]
3. Tsujimoto, Y.; Kamijo, K.; Yoshida, Y. A Theoretical Analysis of Rotating Cavitation in Inducers. *J. Fluids Eng. Trans. ASME* **1993**, *115*, 135–141. [[CrossRef](#)]
4. Watanabe, S.; Sato, K.; Tsujimoto, Y.; Kamijo, K. Analysis of Rotating Cavitation in a Finite Pitch Cascade Using a Closed Cavity Model and a Singularity Method. *J. Fluids Eng. Trans. ASME* **1999**, *121*, 834–840. [[CrossRef](#)]
5. Horiguchi, H.; Watanabe, S.; Tsujimoto, Y. A Linear Stability Analysis of Cavitation in a Finite Blade Count Impeller. *J. Fluids Eng. Trans. ASME* **2000**, *122*, 798–805. [[CrossRef](#)]
6. Cheng, H.; Ji, B.; Long, X.; Huai, W.; Farhat, M. A Review of Cavitation in Tip-Leakage Flow and its Control. *J. Hydrodyn.* **2021**, *33*, 226–242. [[CrossRef](#)]
7. Cheng, H.; Bai, X.; Long, X.; Ji, B.; Peng, X. Large Eddy Simulation of the Tip-Leakage Cavitating Flow with an Insight on how Cavitation Influences Vorticity and Turbulence. *Appl. Math. Model.* **2020**, *77*, 788–809. [[CrossRef](#)]
8. Kang, D.; Yonezawa, K.; Horiguchi, H.; Kawata, Y.; Tsujimoto, Y. Cause of Cavitation Instabilities in Three-Dimensional Inducer. *Int. J. Fluid Mach. Syst.* **2009**, *2*, 206–214. [[CrossRef](#)]
9. Kim, J.; Song, S.J. Visualization of Rotating Cavitation Oscillation Mechanism in a Turbopump Inducer. *J. Fluids Eng. Trans. ASME* **2019**, *141*, 091103. [[CrossRef](#)]
10. Yoon, Y.; Kim, J.; Song, S.J. Identification of Inducer Cavitation Instabilities Using High-Speed Visualization. *Exp. Therm. Fluid Sci.* **2022**, *132*, 110548. [[CrossRef](#)]
11. Huang, J.-D.; Aoki, M.; Zhang, J.-T. Alternate Blade Cavitation on Inducer. *JSME Int. J. Ser. B Fluids Therm. Eng.* **1998**, *41*, 1–6. [[CrossRef](#)]

Disclaimer/Publisher’s Note: The statements, opinions and data contained in all publications are solely those of the individual author(s) and contributor(s) and not of MDPI and/or the editor(s). MDPI and/or the editor(s) disclaim responsibility for any injury to people or property resulting from any ideas, methods, instructions or products referred to in the content.